Noname manuscript No.
(will be inserted by the editor)

Modeling and analysis of passive viscoelastic-legged rimless wheel that generates measurable period of double-limb support

Fumihiko Asano · Junji Kawamoto

Received: date / Accepted: date

Abstract Limit cycle walking including passive-dynamic walkers is generally modeled as a nonlinear hybrid dynamical system with state jumps. The inelastic collision model is usually derived on the assumption that the rear leg leaves the ground immediately after landing of the fore leg. This model is, however, inappropriate in the case of compliant-legged walkers. This paper then reconsiders the traditional collision model and discusses the conditions for transition to double-limb support (DLS) motion which is not instantaneous through investigations of passive dynamic walking of a viscoelastic-legged rimless wheel. First, we experimentally confirm that measurable period of DLS motion emerges after landing of the fore leg, and develop the corresponding mathematical model. Second, we numerically analyze the fundamental properties of the generated passive-dynamic gaits. Furthermore, we discuss the conditions for transition to DLS motion and specify the computational procedures.

Keywords Passive dynamic walking · Double-limb support · Viscoelasticity · Rimless wheel

F. Asano
School of Information Science, Japan Advanced Institute of Science and Technology
1-1 Asahidai, Nomi, Ishikawa 923-1292, Japan
Tel.: +81-761-51-1243
Fax: +81-761-51-1149
E-mail: fasano@jaist.ac.jp

J. Kawamoto
OMRON Corporation
2-2-1 Nishikusatsu, Kusatsu, Shiga 525-0035, Japan
E-mail: junji_kawamoto@omron.co.jp

1 Introduction

Limit cycle walking including passive-dynamic walkers [1] is generally modeled as a nonlinear hybrid dynamical system including state jumps; which consists of the robot equation of motion and transition equations at impacts. The equation of collision is developed as a perfectly inelastic model on the assumption that the previous stance-leg (rear leg) leaves the ground immediately after landing of the next stance-leg (fore leg) [1][2][3]. The period of double-limb support (DLS) then vanishes and the continuous motion consists only of the period of single-limb support (SLS). This model is valid in the case that limit-cycle walkers with rigid leg-frames walk on a rigid ground.

Unlike traditional limit-cycle walkers, compliant-legged walkers are often modeled to generate the period of DLS which is not instantaneous. Using a simple mass-spring model, Geyer et al. numerically showed that the pattern of the ground reaction force (GRF) in the generated gait is significantly similar to that of human walking; there are double-peaks in the vertical GRF [4]. Whittington et al. also performed a related study using an elastic-legged compass-like biped with semicircular feet [5]. The current simulation models are, however, intuitively developed and the condition for transition to DLS motion has not been mathematically identified yet.

It is known that the period of DLS accounts for more than 10% of one cycle in human walking [6][7][8]. In contrast, the period of DLS does not exist in rigid-legged limit cycle walking as mentioned. The properties of DLS must have great effects on the creation of natural, efficient, flexible walking motion of human walking. Also in robot walking, DLS would play important roles in enhancing and improving the gait efficiency and stability. For investigating it, first of all, we should develop the fundamental mathematical model and determine the conditions for transition to DLS motion. It is necessary to reconsider and rewrite the traditional inelastic collision model.

Based on the observations, in this paper we investigate the potentiality and fundamental properties of passive dynamic walking (PDW) including DLS motion which is not instantaneous. As the simplest model for PDW that generates measurable period of DLS, we introduce the model of a planar passive viscoelastic-legged rimless wheel (VRW) that consists of eight identical telescopic-legs incorporating viscoelastic elements. First, we observe the passive-dynamic gait of our experimental machine shown in Fig. 1, and discuss how the traditional collision model should be modified. Second, we develop the mathematical model based on the considerations, and numerically examine the potentiality of stable gait generation including DLS on a gentle slope with commonly-used physical parameters for bipeds. We also numerically analyze the fundamental gait properties and the change of ground reaction force with respect to the viscosity. Furthermore, we mathematically reconsider the conditions for transition to DLS motion and specify the corresponding computational procedures.

This paper is organized as follows. In Section 2, we summarize the experimental results of PDW of our VRW machine. In Section 3, we develop the

Fig. 1 Viscoelastic-legged rimless wheel

mathematical model for numerical simulation following the experimental results. In Section 4, the validity of the model is investigated through numerical simulations. In Section 5, we discuss the conditions for transition to DLS motion. Section 6 concludes this paper and describes future research directions.

2 Experimental results

The experimental VRW shown in Fig. 1 consists of eight identical telescopic-legs incorporating a coil spring. A force due to friction is also derived with the telescopic-leg action. A silicon cap is attached on the end point of the telescopic-leg frames to suppress bouncing at impact. This frame is extended to the end point (maximum length) by the elastic force and is then mechanically locked. The total mass is 4.610 [kg] and the diameter without leg contraction is 0.385 [m].

The telescopic-leg frames can be replaced with rigid-leg ones, and the VRW is also able to generate rigid-legged PDW without measurable period of DLS. By loosening the screw at the central axis, the two identical crossed frames; one is the outside rich-blue frame and the other is the inside light-blue one, can rotate independently and the VRW can behave as a compass-like biped

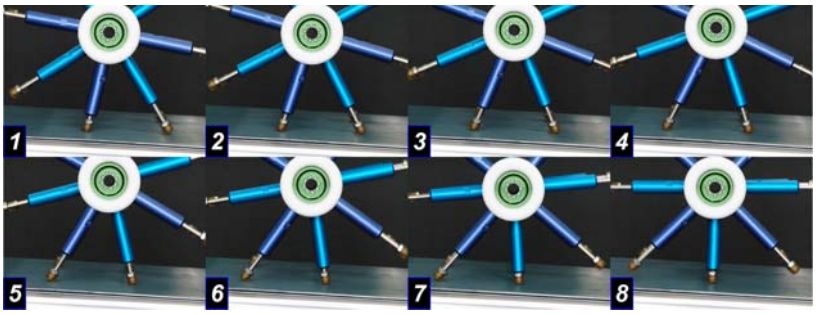

Fig. 2 Snapshots of experimental walking

robot. The center of mass of each leg is, however, positioned at the central axis and the leg's swinging motion does not emerge in the absence of viscosity on the axis [9]. The screw tends to loosen while walking, so we developed and attached a POM (polyacetal) cap for fixing the symmetric configuration.

Using this machine, we conducted an experiment of PDW on a treadmill. Fig. 2 shows the snapshots of the experimental walking on a gentle slope; eight successive pictures taken every 1/60 [s] are laid out in two lines. We can confirm that DLS motion which is not instantaneous emerges after landing of the fore leg (next stance-leg) by using the leg viscoelasticity. The next stance-leg hits the ground and the end point does not bounce nor slip, that is, inelastic collision occurs but the rear leg (current stance-leg) does not leave the ground. The contact condition then changes from SLS to DLS. During the period of DLS, the central position moves along a circular path in accordance with the law of inscribed angle. In this period, the VRW behaves as a 1-DOF system as described later. Soon afterwords the rear leg begins to leave the ground because the ground reaction force perpendicular to the slope reaches zero from positive. After takeoff, the contact condition changes to SLS and the rear leg extends to the end stopper.

In the subsequent sections, we develop the mathematical model and numerically examine the validity. In the simulation studies, however, we consider a larger VRW which can be regarded as the simplified model of human-sized biped walking.

3 Modeling

3.1 Specifications

In this paper, we treat the model of Fig. 3 for analysis and take the following assumptions.

- The model does not have any actuators and is fully passive.
- Each leg frame has viscoelastic elements in the prismatic joint.
- Let m [kg] be the mass of one telescopic-leg frame and m_H [kg] be that of the body frame.

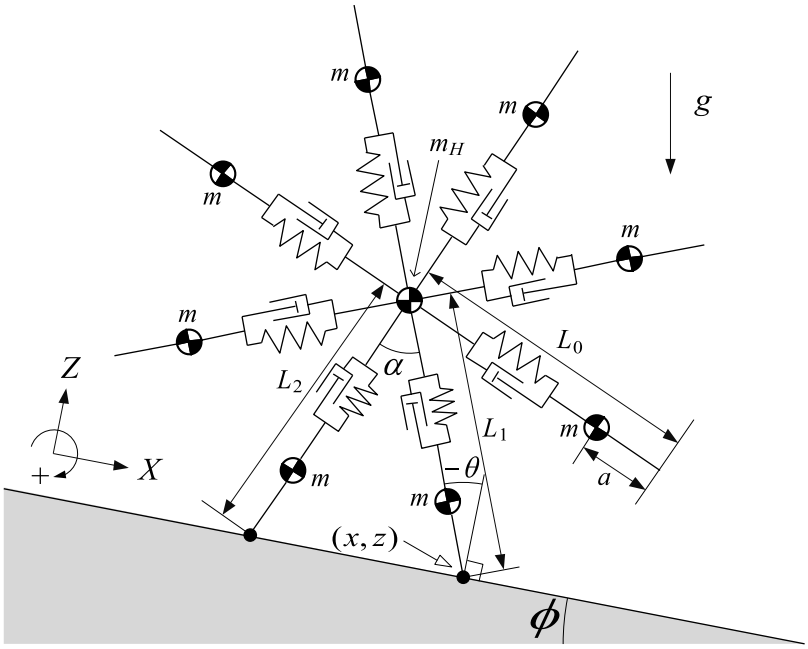

Fig. 3 Model of passive viscoelastic-legged rimless wheel

- The model consists of eight identical leg frames and the shape is symmetry. Therefore all the relative angles between neighboring legs are $\alpha = \pi/4$ [rad].
- The fore and rear legs are called "Leg 1" and "Leg 2".
- Only Leg 1 and Leg 2 expand or contract. The other six legs are mechanically locked by the stopper and their length is kept L_0 [m].
- Let (x, z) and θ [rad] be the end position and vertical angle of Leg 1.
- Let L_j [m] ($j = 1$ or 2) be the length of Leg j.
- Let a [m] be the length between the end point and mass position of each leg frame.

3.2 Equation of motion

Let $\boldsymbol{q}^{\mathrm{T}} = \begin{bmatrix} x & z & \theta & L_1 & L_2 \end{bmatrix}$ be the generalized coordinate vector. The dynamic equation of the VRW then becomes

$$\boldsymbol{M}(\boldsymbol{q})\ddot{\boldsymbol{q}} + \boldsymbol{h}(\boldsymbol{q}, \dot{\boldsymbol{q}}, \phi) = \boldsymbol{\tau}_{\mathrm{ve}}(\boldsymbol{q}, \dot{\boldsymbol{q}}) + \boldsymbol{J}(\boldsymbol{q})^{\mathrm{T}}\boldsymbol{\lambda}, \tag{1}$$

$$\boldsymbol{J}(\boldsymbol{q})\dot{\boldsymbol{q}} = \boldsymbol{0}, \tag{2}$$

where $\boldsymbol{\tau}_{\mathrm{ve}}(\boldsymbol{q}, \dot{\boldsymbol{q}}) \in \mathbb{R}^5$ represents the viscoelastic force that acts on Leg 1 and Leg 2 and is given by

$$\boldsymbol{\tau}_{\mathrm{ve}}(\boldsymbol{q}, \dot{\boldsymbol{q}}) = \begin{bmatrix} \boldsymbol{0}_{3\times 1} \\ -k\left(L_1 - L^*\right) - c\dot{L}_1 \\ -k\left(L_2 - L^*\right) - c\dot{L}_2 \end{bmatrix}. \tag{3}$$

Where k [N/m] is the elastic coefficient, c [N·s/m] is the viscosity coefficient, and L^* [m] is the natural length of the leg frame.

Eq. (2) is the holonomic constraint condition and the Jacobian matrix, $\boldsymbol{J}(\boldsymbol{q})$, changes in accordance with the constraint conditions. By differentiating Eq. (2) with respect to time, we get

$$\boldsymbol{J}(\boldsymbol{q})\ddot{\boldsymbol{q}} + \dot{\boldsymbol{J}}(\boldsymbol{q},\dot{\boldsymbol{q}})\dot{\boldsymbol{q}} = \boldsymbol{0}. \tag{4}$$

Eq. (1) can be arranged as

$$\ddot{\boldsymbol{q}} = \boldsymbol{M}(\boldsymbol{q})^{-1}\left(\boldsymbol{\tau}_{\mathrm{ve}}(\boldsymbol{q},\dot{\boldsymbol{q}}) - \boldsymbol{h}(\boldsymbol{q},\dot{\boldsymbol{q}},\phi)\right) + \boldsymbol{M}(\boldsymbol{q})^{-1}\boldsymbol{J}(\boldsymbol{q})^{\mathrm{T}}\boldsymbol{\lambda}. \tag{5}$$

Following Eq. (4) and (5), we get

$$\begin{aligned}\boldsymbol{J}(\boldsymbol{q})\ddot{\boldsymbol{q}} &= \boldsymbol{J}(\boldsymbol{q})\boldsymbol{M}(\boldsymbol{q})^{-1}\left(\boldsymbol{\tau}_{\mathrm{ve}}(\boldsymbol{q},\dot{\boldsymbol{q}}) - \boldsymbol{h}(\boldsymbol{q},\dot{\boldsymbol{q}},\phi)\right) + \boldsymbol{J}(\boldsymbol{q})\boldsymbol{M}(\boldsymbol{q})^{-1}\boldsymbol{J}(\boldsymbol{q})^{\mathrm{T}}\boldsymbol{\lambda} \\ &= -\dot{\boldsymbol{J}}(\boldsymbol{q},\dot{\boldsymbol{q}})\dot{\boldsymbol{q}}. \end{aligned} \tag{6}$$

The vector $\boldsymbol{\lambda}$ is then solved as

$$\begin{aligned}\boldsymbol{\lambda} = &-\boldsymbol{X}(\boldsymbol{q})^{-1}\boldsymbol{J}(\boldsymbol{q})\boldsymbol{M}(\boldsymbol{q})^{-1}\left(\boldsymbol{\tau}_{\mathrm{ve}}(\boldsymbol{q},\dot{\boldsymbol{q}}) - \boldsymbol{h}(\boldsymbol{q},\dot{\boldsymbol{q}},\phi)\right) \\ &-\boldsymbol{X}(\boldsymbol{q})^{-1}\dot{\boldsymbol{J}}(\boldsymbol{q},\dot{\boldsymbol{q}})\dot{\boldsymbol{q}}, \end{aligned} \tag{7}$$

$$\boldsymbol{X}(\boldsymbol{q}) = \boldsymbol{J}(\boldsymbol{q})\boldsymbol{M}(\boldsymbol{q})^{-1}\boldsymbol{J}(\boldsymbol{q})^{\mathrm{T}}. \tag{8}$$

By eliminating this into Eq. (1), we get

$$\boldsymbol{M}(\boldsymbol{q})\ddot{\boldsymbol{q}} = \boldsymbol{Y}(\boldsymbol{q})\left(\boldsymbol{\tau}_{\mathrm{ve}}(\boldsymbol{q},\dot{\boldsymbol{q}}) - \boldsymbol{h}(\boldsymbol{q},\dot{\boldsymbol{q}},\phi)\right) - \boldsymbol{J}(\boldsymbol{q})^{\mathrm{T}}\boldsymbol{X}(\boldsymbol{q})^{-1}\dot{\boldsymbol{J}}(\boldsymbol{q},\dot{\boldsymbol{q}})\dot{\boldsymbol{q}}, \tag{9}$$

$$\boldsymbol{Y}(\boldsymbol{q}) := \boldsymbol{I}_5 - \boldsymbol{J}(\boldsymbol{q})^{\mathrm{T}}\boldsymbol{X}(\boldsymbol{q})^{-1}\boldsymbol{J}(\boldsymbol{q})\boldsymbol{M}(\boldsymbol{q})^{-1}. \tag{10}$$

3.3 Constraint conditions during stance phase

The passive gait of the VRW consists of the following five phases (See Fig. 4).

1. Collision phase I: Landing of Leg 1
2. Stance phase (DLS): DLS and 1-DOF
3. Stance phase (SLS-I): SLS and 3-DOF
4. Collision phase II: Hitting the stopper of Leg 2
5. Stance phase (SLS-II): SLS and 2-DOF

In the following, the equations of motion according to each constraint condition are described in detail.

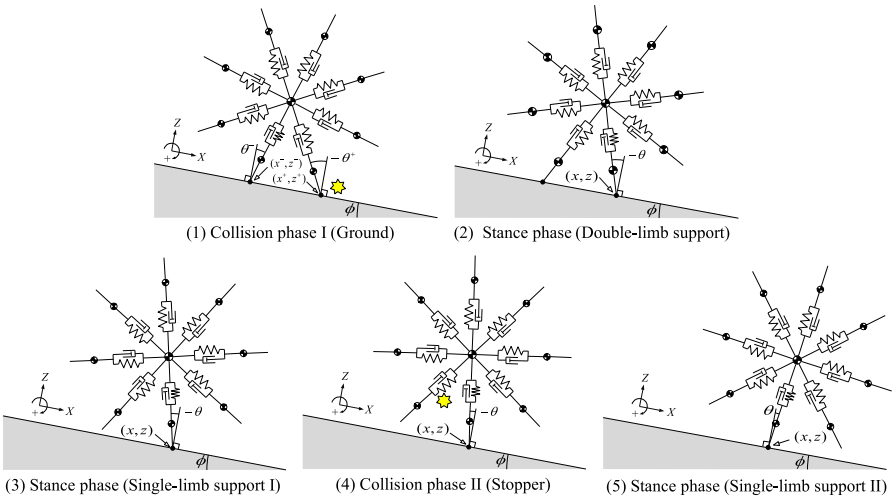

Fig. 4 Motion sequence

3.3.1 Period of double-limb support

In this period, the following two constraint conditions are satisfied.

(a) Leg 1's end contacts with the ground without slipping.
(b) Leg 2's end contacts with the ground without slipping.

The equations for the velocity constraints are written as follows.

$$\begin{aligned} \dot{x} &= 0 \\ \dot{z} &= 0 \\ \frac{\mathrm{d}}{\mathrm{d}t}\left(x + L_1 \sin\theta - L_2 \sin(\theta+\alpha)\right) &= 0 \\ \frac{\mathrm{d}}{\mathrm{d}t}\left(z + L_1 \cos\theta - L_2 \cos(\theta+\alpha)\right) &= 0 \end{aligned}$$

By summarizing these four equations, the Jacobian matrix becomes

$$\boldsymbol{J}(\boldsymbol{q}) = \begin{bmatrix} \boldsymbol{J}_1 \\ \boldsymbol{J}_2 \\ \boldsymbol{J}_3(\boldsymbol{q}) \\ \boldsymbol{J}_4(\boldsymbol{q}) \end{bmatrix} = \begin{bmatrix} 1 & 0 & 0 & 0 & 0 \\ 0 & 1 & 0 & 0 & 0 \\ 1 & 0 & J_{33} & \sin\theta & J_{35} \\ 0 & 1 & J_{43} & \cos\theta & J_{45} \end{bmatrix} =: \boldsymbol{J}_{\mathrm{DLS}}(\boldsymbol{q}), \tag{11}$$

where

$$\begin{aligned} J_{33} &= L_1 \cos\theta - L_2 \cos(\theta+\alpha), \quad J_{35} = -\sin(\theta+\alpha), \\ J_{43} &= -L_1 \sin\theta - L_2 \sin(\theta+\alpha), \quad J_{45} = -\cos(\theta+\alpha). \end{aligned}$$

In this period, the 5-DOF robot equation of motion has four holonomic constraints. The generated motion thus becomes 1-DOF. As previously mentioned, the central position of the VRW moves along a circular orbit.

The holonomic constraint force term in Eq. (1) can be divided into

$$\boldsymbol{J}(\boldsymbol{q})^{\mathrm{T}}\boldsymbol{\lambda} = \boldsymbol{J}_1^{\mathrm{T}}\lambda_1 + \boldsymbol{J}_2^{\mathrm{T}}\lambda_2 + \boldsymbol{J}_3(\boldsymbol{q})^{\mathrm{T}}\lambda_3 + \boldsymbol{J}_4(\boldsymbol{q})^{\mathrm{T}}\lambda_4. \tag{12}$$

The ground reaction force acting on Leg 1's end perpendicular to the slope is λ_2, and that of Leg 2 is λ_4. We can detect the instant of takeoff of Leg 2 by checking the sign of λ_4.

3.3.2 Period of single-limb support I

In this period, only the condition (a) is satisfied. The Jacobian matrix then becomes

$$\boldsymbol{J} = \begin{bmatrix} \boldsymbol{J}_1 \\ \boldsymbol{J}_2 \end{bmatrix} =: \boldsymbol{J}_{\mathrm{SLS}}, \tag{13}$$

where $\boldsymbol{J}_1$ and $\boldsymbol{J}_2$ are the same as those of Eq. (11)

3.3.3 Period of single-limb support II

In this period, the following condition is added.

(c) Leg 2 is fully-extended and immobile (mechanically locked).

This velocity constraint condition is given by $\dot{L}_2 = 0$. The Jacobian matrix then becomes

$$\boldsymbol{J} = \begin{bmatrix} \boldsymbol{J}_1 \\ \boldsymbol{J}_2 \\ 0\ 0\ 0\ 0\ 1 \end{bmatrix} =: \boldsymbol{J}'_{\mathrm{SLS}}. \tag{14}$$

3.4 Collision equations

3.4.1 Landing of Leg 1

As can be seen in Fig. 5, we must replace the position and velocity vectors immediately before impact, $\boldsymbol{q}^-$ and $\dot{\boldsymbol{q}}^-$, with those exchanging Leg 1 and Leg 2 for the next, $\boldsymbol{q}^+$ and $\dot{\boldsymbol{q}}^+$, which are detailed as follows.

$$\boldsymbol{q}^+ = \begin{bmatrix} 0 \\ 0 \\ \theta^- - \alpha \\ L_0 \\ L_1^- \end{bmatrix}, \quad \dot{\boldsymbol{q}}^+ = \begin{bmatrix} \dot{x}^+ \\ \dot{z}^+ \\ \dot{\theta}^- \\ 0 \\ \dot{L}_1^- \end{bmatrix} \tag{15}$$

$$\dot{x}^+ = \dot{x}^- + \left(L_1^- \cos\theta^- - L_0 \cos(\alpha - \theta^-)\right)\dot{\theta}^- + \dot{L}_1 \sin\theta^- \tag{16}$$

$$\dot{z}^+ = \dot{z}^- - \left(L_1^- \sin\theta^- + L_0 \sin(\alpha - \theta^-)\right)\dot{\theta}^- + \dot{L}_1 \cos\theta^- \tag{17}$$

By adding the following assumption, we can derive the inelastic collision model.

(d) Leg 1's end collides with the ground but Leg 2 does not take off.

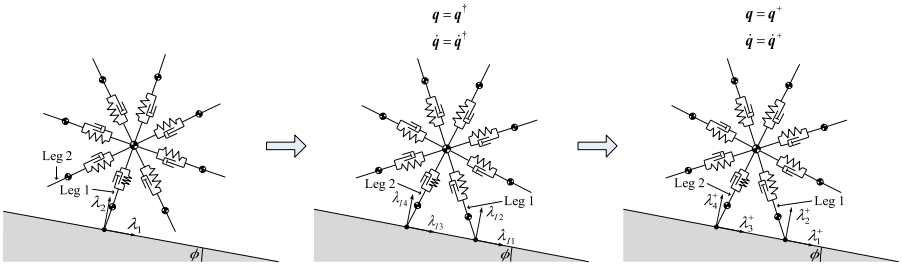

Fig. 5 Coordinate change at collision phase I

The equation is then given by

$$\boldsymbol{M}(\boldsymbol{q}^{\dagger})\dot{\boldsymbol{q}}^{+} = \boldsymbol{M}(\boldsymbol{q}^{\dagger})\dot{\boldsymbol{q}}^{\dagger} + \boldsymbol{J}_I(\boldsymbol{q}^{\dagger})^{\mathrm{T}}\boldsymbol{\lambda}_I, \tag{18}$$

$$\boldsymbol{J}_I(\boldsymbol{q}^{\dagger})\dot{\boldsymbol{q}}^{+} = \boldsymbol{0}_{4\times 1}. \tag{19}$$

Here, note that $\boldsymbol{\lambda}_I$ is the vector obtained by integrating the impulsive force at impact for zero time and therefore the unit of each element is N·s. This is also explained in section 5. In this situation, the constraint conditions are (a) and (b). The Jacobian matrix $\boldsymbol{J}_I(\boldsymbol{q}^{\dagger}) \in \mathbb{R}^{4\times 5}$ is therefore identical to Eq. (11). By solving Eqs. (18) and (19) for the velocity vector immediately after impact, we get

$$\dot{\boldsymbol{q}}^{+} = \left(\boldsymbol{I}_5 - \boldsymbol{M}(\boldsymbol{q}^{\dagger})^{-1}\boldsymbol{J}_I(\boldsymbol{q}^{\dagger})^{\mathrm{T}}\boldsymbol{X}_I(\boldsymbol{q}^{\dagger})^{-1}\boldsymbol{J}_I(\boldsymbol{q}^{\dagger})\right)\dot{\boldsymbol{q}}^{\dagger}, \tag{20}$$

$$\boldsymbol{X}_I(\boldsymbol{q}^{\dagger}) := \boldsymbol{J}_I(\boldsymbol{q}^{\dagger})\boldsymbol{M}(\boldsymbol{q}^{\dagger})^{-1}\boldsymbol{J}_I(\boldsymbol{q}^{\dagger})^{\mathrm{T}}. \tag{21}$$

3.4.2 Collision to stopper of Leg 2

The constraint conditions for this collision are (a), (b), and (c). Therefore the corresponding Jacobian matrix becomes $\boldsymbol{J}'_{\mathrm{SLS}}$ and the inelastic collision is modeled as

$$\boldsymbol{M}(\boldsymbol{q}_s)\dot{\boldsymbol{q}}_s^{+} = \boldsymbol{M}(\boldsymbol{q}_s)\dot{\boldsymbol{q}}_s^{-} + \left(\boldsymbol{J}'_{\mathrm{SLS}}\right)^{\mathrm{T}}\boldsymbol{\lambda}_s, \tag{22}$$

$$\boldsymbol{J}'_{\mathrm{SLS}}\dot{\boldsymbol{q}}_s^{+} = \boldsymbol{0}_{3\times 1}. \tag{23}$$

Here, we denoted the position and velocity vectors at this instant, however, as $\boldsymbol{q}_s$ and $\dot{\boldsymbol{q}}_s$. $\boldsymbol{\lambda}_s \in \mathbb{R}^3$ is the vector obtained by integrating the impulsive force at impact for zero time. We assume that this collision occurs during the period of SLS. By solving Eqs. (22) and (23) for the velocity vector immediately after impact, we get

$$\dot{\boldsymbol{q}}_s^{+} = \left(\boldsymbol{I}_5 - \boldsymbol{M}(\boldsymbol{q}_s)^{-1}\left(\boldsymbol{J}'_{\mathrm{SLS}}\right)^{\mathrm{T}}\boldsymbol{X}_s(\boldsymbol{q}_s)^{-1}\boldsymbol{J}'_{\mathrm{SLS}}\right)\dot{\boldsymbol{q}}_s^{-}, \tag{24}$$

$$\boldsymbol{X}_s(\boldsymbol{q}_s) := \boldsymbol{J}'_{\mathrm{SLS}}\boldsymbol{M}(\boldsymbol{q}_s)^{-1}\left(\boldsymbol{J}'_{\mathrm{SLS}}\right)^{\mathrm{T}}. \tag{25}$$

Note that this collision occurs only in the case that the natural length, L^*, is longer than the nominal length, L_0.

3.5 Mechanical energy

The total mechanical energy of the VRW is determined as

$$E(\boldsymbol{q}, \dot{\boldsymbol{q}}) = \frac{1}{2}\dot{\boldsymbol{q}}^{\mathrm{T}}\boldsymbol{M}(\boldsymbol{q})\dot{\boldsymbol{q}} + P(\boldsymbol{q}), \tag{26}$$

where the potential energy, $P(\boldsymbol{q})$, is the sum of energies of position and elasticity. The elastic energy is given by

$$\frac{1}{2}k\left(L_1 - L^*\right)^2 + \frac{1}{2}k\left(L_2 - L^*\right)^2 + 3k\left(L_0 - L^*\right)^2. \tag{27}$$

The viscous dissipation function, $R(\dot{\boldsymbol{q}})$, is given by

$$R(\dot{\boldsymbol{q}}) = \frac{1}{2}c\left(\dot{L}_1^2 + \dot{L}_2^2\right), \tag{28}$$

and the damping force then dissipates mechanical energy as

$$\dot{E} = -\dot{\boldsymbol{q}}^{\mathrm{T}}\frac{\partial R(\dot{\boldsymbol{q}})}{\partial \dot{\boldsymbol{q}}^{\mathrm{T}}} = -c\left(\dot{L}_1^2 + \dot{L}_2^2\right) \leq 0. \tag{29}$$

The total mechanical energy then monotonically decreases during motion.

4 Typical gaits

Fig. 6 shows the simulation results of PDW of the VRW on a slope where $\phi = 0.30$ [rad]. The physical parameters were chosen as listed in Table 1. The nominal leg length, L_0, was chosen by reference to the biped models in related works [4][5]. The generated motion can then be regarded as the human-sized bipedal gait without swing-leg motion. Fig. 7 plots the stick diagram of the steady gait in X-Z plane; Leg 1 and Leg 2 are respectively depicted by the solid and dotted lines.

We can see the following characteristics in each figure.

(a) The angle monotonically increases during the stance phases.
(b) Leg 1 monotonically contracts after landing, while Leg 2 monotonically extends and finally collides the stopper.
(c) The distribution of the ground reaction force perpendicular to the slope shifts from the rear leg (Leg 2) to the fore one (Leg 1) soon after the collision phase I. The period of DLS accounts for about 53 % of one cycle.
(d) The position of Leg 2's end monotonically moves upward after the collision phase II.

From Fig. 6(e), we can see that λ_2 discontinuously changes at the instant that the motion transitions from DLS to SLS. This is because λ_3 (ground reaction force of Leg 2 parallel to the slope) jumps from nonzero to zero at this instant. Unlike the simple spring-mass walkers [4][5], there is only one force-peak during one cycle.

Table 1 Physical parameter settings

m_H	10.0	kg	L_0	1.0	m
m	1.0	kg	L^*	1.02	m
α	$\pi/4$	rad	k	500	N/m
a	0.3	m	c	200	N·s/m

Fig. 8 shows the time evolutions of the end position of Leg 2 for three values of c. If c is small, Leg 2 rapidly extends immediately after takeoff and the end position hits the ground. Except the case of $c = 200$, Leg 2 hits the ground during the stance phase of SLS-I. The leg viscosity controls the extension speed of the telescopic-leg frame and must be chosen carefully to avoid the hitting.

Fig. 9 shows the ground reaction force perpendicular to the slope of Leg 2, λ_4, for three values of c. We can see that the value immediately after collision phase I, λ_4^+, approaches to zero as c increases. If c increases further, the value reaches zero and Leg 2 cannot maintain contact with the ground immediately after impact. The Leg 2 will leave the ground immediately after impact, and the ground reaction force completely shifts from Leg 2 to Leg 1. This corresponds to the traditional inelastic collision model for stance-leg exchange [1][2][3]. Large c intends that the deformation velocity of the compliant leg frames is low. This implies that the traditional collision model that does not generate measurable period of DLS is reasonable in the case with difficulty deformable compliant leg frames. In addition, note that the slope was chosen as 0.30 [rad] and this is much steeper than the available slope for passive compass-like walkers [2] and rimless wheels [10] that consist of rigid-leg frames. This implies that viscoelastic-legged walkers need sufficiently large driving force in the walking direction.

On the other hand, it has been pointed out that there are two peaks of the vertical ground reaction force in level dynamic walking of a simple spring-mass model [4][5]. In our model, however, only one peak is found in the case of $c = 200$. A number of reasons can be given for this difference; existence of leg mass, effect of viscosity, magnitude of the slope, and so on. Now we are investigating the mathematical reason from various point of views.

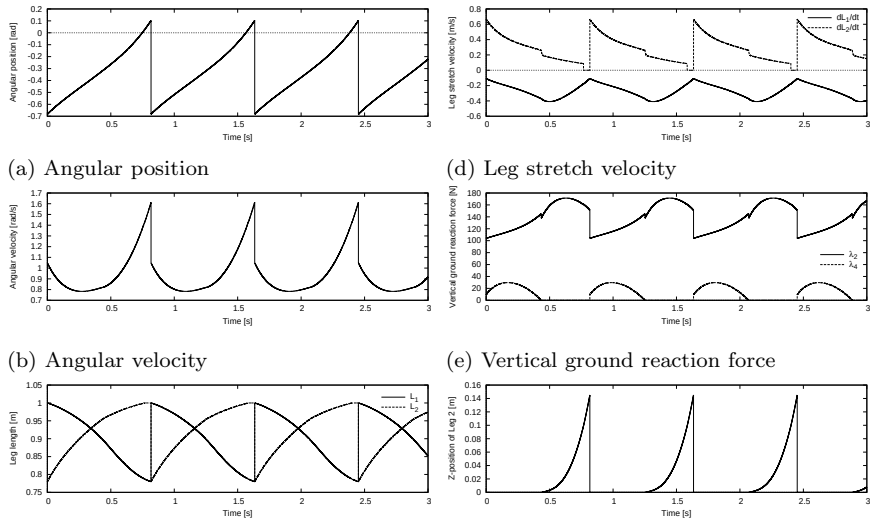

(a) Angular position (d) Leg stretch velocity

(b) Angular velocity (e) Vertical ground reaction force

(c) Leg length (f) Z-position of end-point of Leg 2

Fig. 6 Simulation results of passive dynamic walking

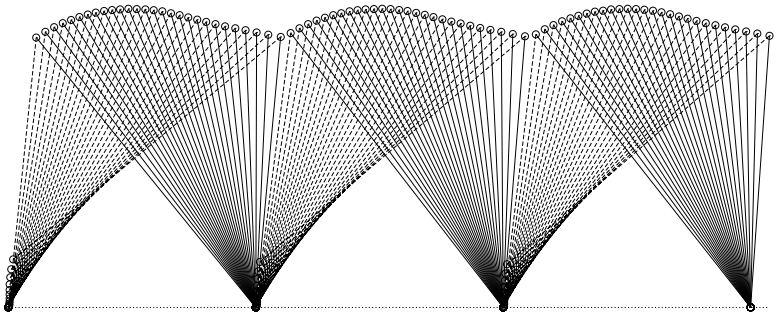

Fig. 7 Stick diagram of steady gait

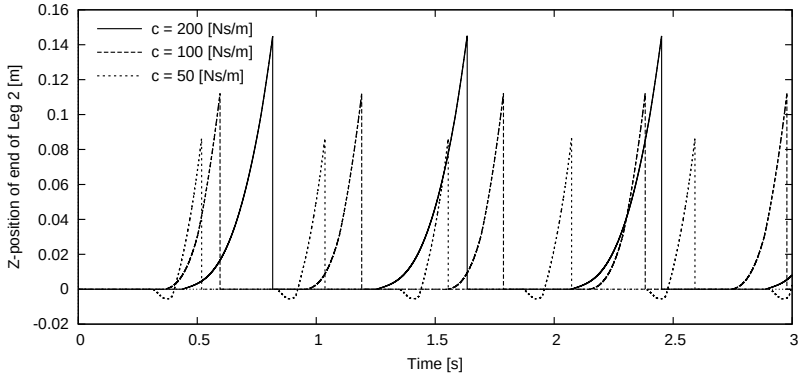

Fig. 8 Time evolution of Z-position of Leg 2's end

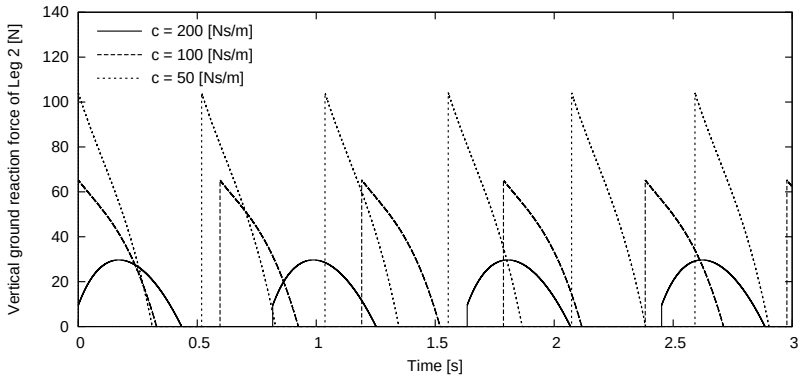

Fig. 9 Time evolution of ground reaction force perpendicular to slope

5 Indicators for emergence of double-limb support

In the previous section, we intuitively performed numerical simulations on the assumption that Leg 2 does not leave the ground immediately after touchdown of Leg 1. This section reconsiders the validity and defines the conditions for transition to DLS motion.

5.1 DLS-Indicators and computational procedures

Let $\boldsymbol{f}$ be the vector of ground reaction force on the contact points of Leg 1 and Leg 2 at impact, and $\boldsymbol{J}_I(\boldsymbol{q})$ be the corresponding Jacobian matrix. The equation of motion then becomes

$$\boldsymbol{M}(\boldsymbol{q})\ddot{\boldsymbol{q}} + \boldsymbol{h}(\boldsymbol{q}, \dot{\boldsymbol{q}}, \phi) = \boldsymbol{\tau}_{\mathrm{ve}}(\boldsymbol{q}, \dot{\boldsymbol{q}}) + \boldsymbol{J}_I(\boldsymbol{q})^{\mathrm{T}} \boldsymbol{f}. \tag{30}$$

Let $\boldsymbol{q}^\dagger$ and $\dot{\boldsymbol{q}}^\dagger$ be the vectors defined in Eq. (15). Note that $\boldsymbol{q}^\dagger = \boldsymbol{q}^- = \boldsymbol{q}^+$ holds. We assume that the touchdown of Leg 1 occurs at $t = T_0$ [s], that is, $\boldsymbol{q}^\dagger = \boldsymbol{q}(T_0)$. The time integral of the left-hand side of Eq. (30) then becomes

$$\begin{aligned}\lim_{\varepsilon\to+0}\int_{T_0-\frac{\varepsilon}{2}}^{T_0+\frac{\varepsilon}{2}} \left(\boldsymbol{M}(\boldsymbol{q})\ddot{\boldsymbol{q}} + \boldsymbol{h}(\boldsymbol{q},\dot{\boldsymbol{q}},\phi)\right) \mathrm{d}t &= \int_{T_0^-}^{T_0^+} \boldsymbol{M}(\boldsymbol{q}^\dagger)\ddot{\boldsymbol{q}}\ \mathrm{d}t \\ &= \boldsymbol{M}(\boldsymbol{q}^\dagger)\left(\dot{\boldsymbol{q}}^+ - \dot{\boldsymbol{q}}^\dagger\right), \end{aligned} \tag{31}$$

whereas the time integral of the right-hand side becomes

$$\begin{aligned}\lim_{\varepsilon\to+0}\int_{T_0-\frac{\varepsilon}{2}}^{T_0+\frac{\varepsilon}{2}} \left(\boldsymbol{\tau}_{\mathrm{ve}}(\boldsymbol{q},\dot{\boldsymbol{q}}) + \boldsymbol{J}_I(\boldsymbol{q})^{\mathrm{T}}\boldsymbol{f}\right) \mathrm{d}t &= \boldsymbol{J}_I(\boldsymbol{q}^\dagger)^{\mathrm{T}} \lim_{\varepsilon\to+0}\int_{T_0-\frac{\varepsilon}{2}}^{T_0+\frac{\varepsilon}{2}} \boldsymbol{f}\ \mathrm{d}t \\ &= \boldsymbol{J}_I(\boldsymbol{q}^\dagger)^{\mathrm{T}}\boldsymbol{\lambda}_I. \end{aligned} \tag{32}$$

The collision equation then becomes

$$\boldsymbol{M}(\boldsymbol{q}^\dagger)\dot{\boldsymbol{q}}^+ = \boldsymbol{M}(\boldsymbol{q}^\dagger)\dot{\boldsymbol{q}}^\dagger + \boldsymbol{J}_I(\boldsymbol{q}^\dagger)^{\mathrm{T}}\boldsymbol{\lambda}_I, \tag{33}$$

$$\boldsymbol{J}_I(\boldsymbol{q}^\dagger)\dot{\boldsymbol{q}}^+ = \boldsymbol{0}. \tag{34}$$

Eq. (33) is the same as Eq. (18) but the size of the Jacobian matrix at impact, $\boldsymbol{J}_I(\boldsymbol{q}^\dagger)$, and the dimension of Eq. (34) are exchanged in accordance with the following algorithm.

Computational procedure for determining $\dot{\boldsymbol{q}}^+$

(A1) We set $\boldsymbol{J}_I(\boldsymbol{q}^\dagger) = \boldsymbol{J}_{\mathrm{DLS}}(\boldsymbol{q}^\dagger)$ in Eq. (34) and compute the Lagrange undetermined multiplier vector in Eq. (33), $\boldsymbol{\lambda}_I \in \mathbb{R}^4$. This is solved as

$$\boldsymbol{\lambda}_I = \left(\boldsymbol{I}_5 - \boldsymbol{M}(\boldsymbol{q}^\dagger)^{-1}\boldsymbol{J}_I(\boldsymbol{q}^\dagger)^{\mathrm{T}}\boldsymbol{X}_I(\boldsymbol{q}^\dagger)^{-1}\boldsymbol{J}_I(\boldsymbol{q}^\dagger)\right)\dot{\boldsymbol{q}}^\dagger, \tag{35}$$

where $\boldsymbol{X}_I(\boldsymbol{q}^\dagger)$ is identical to Eq. (21).

(A2) Divide the obtained $\boldsymbol{\lambda}_I$ into $\boldsymbol{\lambda}_I = \begin{bmatrix}\lambda_{I1} & \lambda_{I2} & \lambda_{I3} & \lambda_{I4}\end{bmatrix}^{\mathrm{T}}$. $\lambda_{I2} \geq 0$ and $\lambda_{I4} \geq 0$ must hold to transition to DLS motion. It is obvious, however, that $\lambda_{I2} > 0$ always holds. Therefore we should check the sign of λ_{I4} only.

(A3) If $\lambda_{I4} < 0$, DLS motion does not emerge. We then solve Eqs. (33) and (34) for $\dot{\boldsymbol{q}}^+$ by setting $\boldsymbol{J}(\boldsymbol{q}^\dagger) = \boldsymbol{J}_{\mathrm{SLS}}$.

(A4) If $\lambda_{I4} \geq 0$, the motion then transitions to DLS. We then solve Eqs. (33) and (34) for $\dot{\boldsymbol{q}}^+$ by setting $\boldsymbol{J}(\boldsymbol{q}^\dagger) = \boldsymbol{J}_{\mathrm{DLS}}(\boldsymbol{q}^\dagger)$.

Here, note that the unit of each component of $\boldsymbol{\lambda}_I$ is N·s because this is time-integral of the impulsive force, $\boldsymbol{f}$, as suggested by Eq. (32). The component of $\boldsymbol{\lambda}_I$ is positive means, however, the average value of the corresponding impulsive ground reaction force during zero-time interval is positive. Therefore λ_{I4} [N·s] can be treated in the same manner as the corresponding ground reaction force, λ_4 [N].

Leg 2 begins to leave the ground at the instant that the sign of λ_4 in Eq. (12) continuously changes from positive to negative. The problem is that λ_4 immediately after impact, λ_4^+, does not always become positive even if λ_{I4} is positive in the case that the collision occurs while exerting the viscoelastic force. We therefore consider the following computational procedure.

Computational procedure for determining $\ddot{\boldsymbol{q}}^+$

(B1) If $\lambda_{I4} \geq 0$, the motion is determined to transition to DLS. The equations of motion immediately after impact are then specified as

$$\boldsymbol{M}(\boldsymbol{q}^\dagger)\ddot{\boldsymbol{q}}^+ + \boldsymbol{h}(\boldsymbol{q}^\dagger, \dot{\boldsymbol{q}}^+, \phi) = \boldsymbol{\tau}_{\rm ve}(\boldsymbol{q}^\dagger, \dot{\boldsymbol{q}}^+) + \boldsymbol{J}_{\rm DLS}(\boldsymbol{q}^\dagger)^{\rm T}\boldsymbol{\lambda}^+, \tag{36}$$

$$\boldsymbol{J}_{\rm DLS}(\boldsymbol{q}^\dagger)\dot{\boldsymbol{q}}^+ = \boldsymbol{0}_{4\times 1}, \tag{37}$$

by using $\dot{\boldsymbol{q}}^+$ obtained in (A4). We can solve Eqs. (36) and (37) for $\boldsymbol{\lambda}^+ \in \mathbb{R}^4$ as

$$\boldsymbol{\lambda}^+ = -\boldsymbol{X}(\boldsymbol{q}^\dagger)^{-1}\left(\boldsymbol{J}_{\rm DLS}(\boldsymbol{q}^\dagger)\boldsymbol{M}(\boldsymbol{q}^\dagger)^{-1}\left(\boldsymbol{\tau}_{\rm ve}(\boldsymbol{q}^\dagger, \dot{\boldsymbol{q}}^+) - \boldsymbol{h}(\boldsymbol{q}^\dagger, \dot{\boldsymbol{q}}^+, \phi)\right) + \dot{\boldsymbol{J}}_{\rm DLS}(\boldsymbol{q}^\dagger, \dot{\boldsymbol{q}}^+)\dot{\boldsymbol{q}}^+\right). \tag{38}$$

$\ddot{\boldsymbol{q}}^+$ is then immediately calculated by substituting this into Eq. (36).

(B2) Divide the obtained $\boldsymbol{\lambda}^+$ into $\boldsymbol{\lambda}^+ = \left[\lambda_1^+ \ \lambda_2^+ \ \lambda_3^+ \ \lambda_4^+\right]^{\rm T}$. If $\lambda_2^+ \geq 0$ and $\lambda_4^+ \geq 0$, then we take $\ddot{\boldsymbol{q}}^+$ obtained in (B1) as the proper initial acceleration vector and continue the numerical integral. A measurable period of DLS motion emerges.

(B3) If $\lambda_2^+ \geq 0$ and $\lambda_4^+ < 0$, unilateral constraint condition is not satisfied and the motion should transition to SLS. We then break $\ddot{\boldsymbol{q}}^+$ obtained in (B1), and solve the following equations

$$\boldsymbol{M}(\boldsymbol{q}^\dagger)\ddot{\boldsymbol{q}}^+ + \boldsymbol{h}(\boldsymbol{q}^\dagger, \dot{\boldsymbol{q}}^+, \phi) = \boldsymbol{\tau}_{\rm ve}(\boldsymbol{q}^\dagger, \dot{\boldsymbol{q}}^+) + \boldsymbol{J}_{\rm SLS}^{\rm T}\boldsymbol{\lambda}^+ \tag{39}$$

$$\boldsymbol{J}_{\rm SLS}\dot{\boldsymbol{q}}^+ = \boldsymbol{0}_{2\times 1}, \tag{40}$$

for $\boldsymbol{\lambda}^+ \in \mathbb{R}^2$ and $\ddot{\boldsymbol{q}}^+$. Here, $\boldsymbol{\lambda}^+$ is calculated by replacing $\boldsymbol{J}_{\rm DLS}(\boldsymbol{q}^\dagger)$ and $\dot{\boldsymbol{J}}_{\rm DLS}(\boldsymbol{q}^\dagger, \dot{\boldsymbol{q}}^\dagger)$ in Eq. (38) by $\boldsymbol{J}_{\rm SLS}$ and $\boldsymbol{0}_{2\times 5}$. We take this newly-calculated acceleration vector as the proper initial one, and begin the numerical integral.

The measurable period of DLS emerges immediately after impact if λ_{I4}, λ_2^+, and λ_4^+ are positive. These three quantities are thus termed as the DLS-Indicator (DLSIs).

5.2 Analysis of DLSIs

Fig. 10 plots the DLSIs with respect to the leg viscosity, c, in PDW on the slope of $\phi = 0.10$ [rad]. The physical parameters except c were chosen as listed in Table 1. Here, (a) plots λ_{I4} and (b) plots λ_2^+ and λ_4^+. We also plotted their

values with different symbols in the case that scuffing of Leg 2 arises; the rear leg quickly extends after takeoff where c is small and the end-point hits the ground. Our mathematical model cannot deal with bouncing of Leg 1 and scuffing of Leg 2. We therefore plotted only the case where $\lambda_2^+ \geq 0$ and omitted the effect of scuffing of Leg 2 in the numerical simulations. All the DLSIs are positive where $c = 50$, 100, and 200 [N·s/m]. Therefore we can confirm that the simulation results performed in the previous section were valid except scuffing.

As seen from Fig. 10 (b), λ_4^+ monotonically decreases as c increases and finally reaches zero where $c = 220$ [N·s/m]. $\lambda_4^+ < 0$ implies that unilateral constraint of Leg 2 immediately after impact does not hold and the stance-leg exchange is then completed instantaneously where $c \geq 220$. This also implies that the normal velocity of the end-point of Leg 2 immediately after impact is positive. λ_{I4} is, however, always positive as shown in Fig. 10 (a). The Jacobian matrix in Eqs. (33) and (34) is therefore always chosen as $\boldsymbol{J}_I(\boldsymbol{q}^\dagger) = \boldsymbol{J}_{\mathrm{DLS}}(\boldsymbol{q}^\dagger)$.

Bourgeot et al. investigated the condition for transition to DLS and theoretically clarified that there are four possible situations immediately after impact according to the relation between the pre- and post-impact velocities [11]. They mathematically derived how the post-impact situations are determined based on the concept of the rocking block. Font-Llagunes and Kövecses analyzed the condition in passive compass-like biped robot based on a similar approach [12]. They used the post-impact normal velocity of the trailing foot (the end-point of the rear leg) as DLSI. Our analysis results, however, indicate that the following two conditions are not equivalent in the presence of redundant DOFs.

(C1) The normal velocity of the end-point of the rear leg immediately after impact is negative.
(C2) The impulse of the rear leg at impact is positive.

The VRW can generate stable PDW gaits even in the case where $c \geq 220$ but we omitted the plot because the generated gaits are unrealistic and are not 1-period. On the other hand, λ_2^+ monotonically decreases as c decreases and finally reaches zero where $c = 4.0$ [N·s/m]. This implies that bouncing of Leg 1 arises where $c \leq 4.0$.

6 Conclusion and future work

In this paper, we developed a mathematical model for the passive VRW following the experimental results and numerically analyzed the fundamental gait properties. Throughout numerical investigations, we showed that stable gaits including measurable period of DLS can be generated in the presence of large driving force in the walking direction. Furthermore, we mathematically investigated the conditions for transition to DLS motion and specified the corresponding computational procedures.

As the analysis of DLSIs suggested, the stance-leg exchange becomes to terminate instantaneously where c is large because λ_4^+ reaches zero. In this

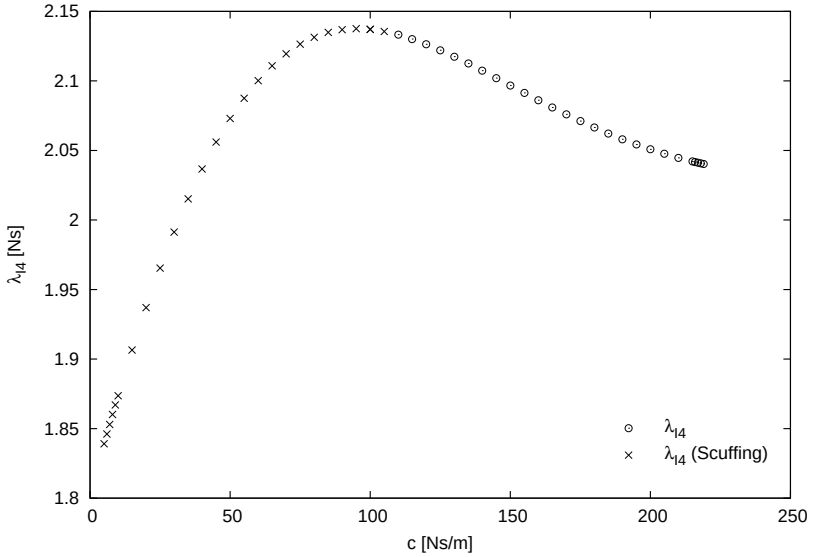

(a) λ_{I4}

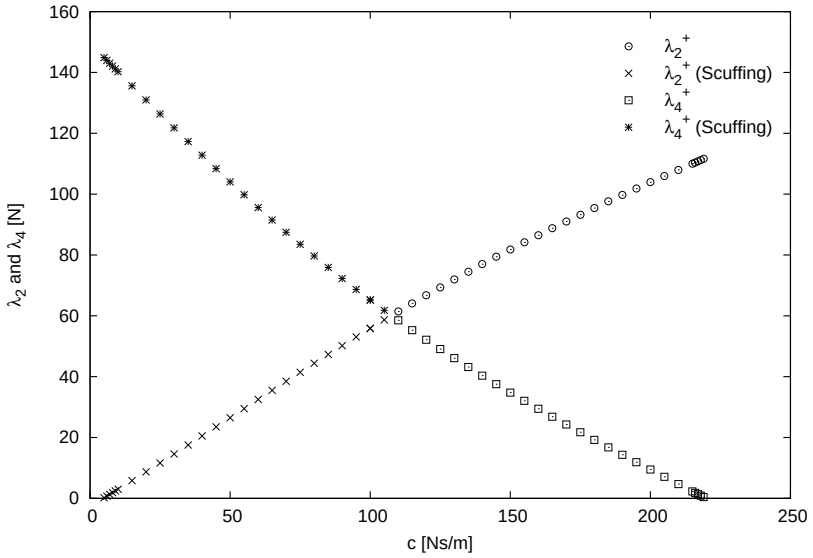

(b) λ_2^+ and λ_4^+

Fig. 10 Double-limb support indicators with respect to c

case, Leg 2 begins to extend and hits the ground immediately after the stance-leg exchange. This leads the next collision of Leg 2 soon after takeoff, and complicated motion is then caused as the result of it. The mathematical model and the corresponding computational procedure in this paper cannot deal with

this situation. They are also not able to deal with the case of bouncing where c is small. We should try to develop the appropriate models in the future.

The contribution of this paper is to have clarified that measurable period of DLS motion emerges in PDW of the VRW and showed how it should be mathematically modeled and simulated. The benefit of the compliance the leg viscoelasticity creates, however, has not been discussed in detail. In the future, we should consider how the evaluation indices should be defined and investigate what effects and advantages DLS motion had on the gait properties.

Acknowledgements The authors wish to thank ONO-DENKI CO., LTD. for many helpful suggestions and technical supports in development of the experimental machine. This research was partially supported by a Grant-in-Aid for Scientific Research, (C) No. 24560542, provided by the Japan Society for the Promotion of Science (JSPS).

References

1. T. McGeer, "Passive dynamic walking," *Int. J. of Robotics Research*, vol. 9, no. 2, pp. 62–82, 1990.
2. A. Goswami, B. Thuilot and B. Espiau, "A study of the passive gait of a compass-like biped robot: Symmetry and chaos," *Int. J. of Robotics Research*, Vol. 17, No. 12, pp. 1282–1301,1998.
3. M. J. Coleman, A. Chatterjee and A. Ruina, "Motions of a rimless spoked wheel: a simple three-dimensional system with impacts," *Dynamics and Stability of Systems*, Vol. 12, No. 3, pp. 139–159, 1997.
4. H. Geyer, A. Seyfarth and R. Blickhan, "Compliant leg behaviour explains basic dynamics of walking and running," *Proc. of the Royal Society B*, Vol. 273, No. 1603, pp. 2861–2867, 2006.
5. B. R. Whittington and D. G. Thelen, "A simple mass-spring model with roller feet can induce the ground reactions observed in human walking," *J. of Biomechanical Engineering*, Vol. 131, Issue 1, pp. 011013-1–011013-8, 2009.
6. M. W. Whittle, *Gait analysis: an introduction*, Butterworth-Heinemann, 2001.
7. M. P. Murray, A. B. Drought and R. C. Kory, "Walking patterns of normal men," *The J. of Bone and Joint Surgery*, vol. 46, no. 2, pp. 335–360, 1964.
8. M. Bouysset, Y. Tourné and K. Tillmann, *Foot and ankle in rheumatoid arthritis*, Springer, 2005.
9. F. Asano, "Simulation and experimental studies on passive-dynamic walker that consists of two identical crossed frames," *Proc. of the IEEE Int. Conf. on Robotics and Automation*, pp. 1703–1708, 2010.
10. F. Asano, "Efficiency and optimality of two-period limit cycle walking," *Advanced Robotics*, Vol. 26, No. 1–2, pp. 155–176, 2012.
11. J.-M. Bourgeot, C. Canudas-de-Wit and B. Brogliato, "Impact shaping for double support walk: from the rocking block to the biped robot," *Proc. of the 8th Int. Conf. on Climbing and Walking Robots and the Support Technologies for Mobile Robots*, London, UK, pp. 509–516, 2005.
12. J. M. Font-Llagunes and J. Kövecses, "Dynamics and energetics of a class of bipedal walking systems," *Mechanism and Machine Theory*, Vol. 44, Iss. 11, pp. 1999–2019, 2009.